

A Modulation Signal Bispectrum Enhanced Squared Envelope for the detection and diagnosis of compound epicyclic gear faults

Structural Health Monitoring
2022, Vol. 0(0) 1–19
© The Author(s) 2022



Article reuse guidelines:
sagepub.com/journals-permissions
DOI: 10.1177/14759217221098577
journals.sagepub.com/home/shm



Yuandong Xu¹ , Guojin Feng², Xiaoli Tang³, Shixi Yang⁴, Fengshou Gu⁵ and Andrew D Ball⁵

Abstract

Epicyclic gearboxes are prevalent in a variety of important engineering systems such as automotive, aerospace, wind turbines, civil equipment and industrial robots owing to the merits of compact structure and high power density. To ensure the productivities of such important systems, condition monitoring techniques are being actively studied to resolve the challenge of varying transmission paths and multiple modulations in vibration signals acquired from ring gear housing. This paper proposes a new Modulation Signal Bispectrum (MSB) Enhanced Squared Envelope method to analyse the vibration signals acquired by a special On-Rotor Sensing (ORS) transducer that is mounted on the shaft of an epicyclic gearbox. A vibration signal model of ORS measurements from epicyclic gearboxes is presented to show the multiple modulation influences. Moreover, inevitable noise influences are also investigated on the conventional squared envelope and the state-of-the-art spectral correlation analysis. On this base, MSB is introduced to suppress these influences for accurately extracting equally spaced harmonics in the squared envelope and is then integrated to isolate fault signatures, allowing effective fault detection and diagnosis of epicyclic gearboxes, which lead to novel contributions of an MSB Enhanced Squared Envelope (MSB-ESE) approach. An experimental study of compound epicyclic gear faults was conducted to demonstrate the superior performance of MSB-ESE along with the special ORS technique in detecting and diagnosing the compound faults on sun and planet gears.

Keywords

Epicyclic gearbox, On-Rotor Sensing, MSB, squared envelope, fault diagnosis

Introduction

Epicyclic gearboxes are widely used in critical machines like wind turbines and aircrafts owing to the unique merits of large transmission ratios and strong torque bearing capacity. Epicyclic gearboxes are usually working at rough conditions and the elements including gears and bearings are vulnerable to various faults, for instance, pitting and fatigue cracks. Fault detection and diagnosis of epicyclic gearboxes at early stages are substantially desired to increase machine reliability and prevent machine failures.

Fault detection and diagnosis of epicyclic gearboxes have attracted substantial attention.¹ Compared with the fixed-axis gearboxes, it is more problematic to detect and diagnose the incipient faults in epicyclic gearboxes because the varying rotating centres of planet gears include the diverging transmission path of the gear sets. Vibration-based monitoring techniques have been advanced significantly in the last two decades. Large quantities of research

were carried out based on the vibration signals obtained from the gearbox housing. Inalpolat and Kahraman² explained the modulation mechanisms of the sidebands in vibration signals from an epicyclic gearbox. They explained the amplitude modulation due to the carrier rotation in the health condition; however, the change when gear faults occur induced additional

¹Dynamics Group, Department of Mechanical Engineering, Imperial College London, London, UK

²School of Mechanical Engineering, Hebei University of Technology, Tianjin, China

³School of Engineering and Technology, Aston University, Birmingham, UK

⁴School of Mechanical Engineering, Zhejiang University, Hangzhou, China

⁵Centre for Efficiency and Performance Engineering, University of Huddersfield, Huddersfield, UK

Corresponding author:

Xiaoli Tang, School of Engineering and Technology, Aston University, Aston St., Birmingham B4 7ET, UK

Email: x.tang4@aston.ac.uk

frequency modulation is not included in the models. With the following investigation, Inalpolat and Kahraman³ developed a nonlinear time-varying dynamic model to explain the sidebands due to amplitude and phase modulation in vibration signals due to manufacturing errors.

Feng and Zuo⁴ proposed the on-housing vibration signal models of the common epicyclic gearbox faults. The signal model considers the local amplitude modulation (AM) and phase modulation (PM) effects and the signal propagating paths when gear fault occurs. These studies explained the vibration signals obtained from the stationary part, typically the housing or ring gear. Given that On-Rotor Sensing is a novel measurement method, modulation phenomena in vibration signals captured from the rotating parts are not well characterised in literature, which will be analytically explained in this paper.

Large quantities of advanced signal processing methods are proposed to monitor the health conditions of epicyclic gearboxes through vibration signals obtained from gearbox housing. Blunt and Keller⁵ introduced two novel methods of synchronous average analysis of the vibration signals for diagnosing the fatigue crack in the carrier of an epicyclic transmission system. The vibration signals of faulty epicyclic gearboxes are rich in discrete components due to both amplitude modulation (AM) and phase modulation (PM) induced by gear defects and the additional amplitude modulation from the periodic varying transmission paths. Feng et al.⁶ used an ensemble empirical mode decomposition (EEMD) method to decompose vibration signals into multiple monocomponent signals for accurate amplitude and frequency demodulation analysis. The developed approach is verified by the simulation and the experimental studies of a wind turbine epicyclic gearbox. With further studies, Feng et al.⁷ developed a joint amplitude and frequency demodulation method based on local mean decomposition (LMD) to extract the characteristic fault frequencies of epicyclic gears. Wang et al.⁸ developed a meshing resonance-based filtering algorithm to detect the ring gear faults. This method can highlight the fault information without using a baseline signal while neglecting other undesired responses. Nonstationary working conditions are a typical case in epicyclic gearboxes and many emerging methods are developed to characterise the nonstationary vibration signals. Vibration responses from epicyclic gearboxes under nonstationary working conditions are time-varying in nature and the varying multicomponents and strong background noise are the critical challenges for fault detection and diagnosis. Feng et al.⁹ proposed iterative generalised demodulation without the need for tacho signals for monitoring epicyclic gearboxes under nonstationary conditions. Compared with the order tracking methods, the generalised demodulation based approaches can avoid the interpolation errors in the step of angular resampling. Sawalhi, Randall and Forrester¹⁰

proposed a tacholess order tracking method to separate the gear and bearing fault signals for diagnosing epicyclic gearboxes in wind turbines. Hou et al.¹¹ improved the generalised demodulation using dual path optimisation ridge estimation, leading to a tacholess order tracking approach in fault detection of wind turbine epicyclic gearboxes.

Despite the advanced demodulation and decomposition methods, envelope analysis is still popular in fault diagnosis of epicyclic gearboxes. Due to time-varying transmission paths, the time-synchronous averaging (TSA) method is not sufficiently capable to improve the signal-noise ratio (SNR) of vibrations. Guo et al.¹² proposed an envelope signal based TSA method to maximise fault signature strength. Wang, Shao and Cao¹³ pointed that the envelope analysis cannot effectively distinguish the fault signatures from the unrelated modulation components. To improve the diagnostic performance of envelope analysis, a genetic algorithm based sub-band selection method was developed to determine the optimal demodulation frequency band for sun gear crack diagnosis. Mauricio and co-authors¹⁴ implemented the cyclostationary analysis to diagnose the bearing faults in an epicyclic gearbox from a wind turbine. The enhanced envelope spectrum is a promising approach for monitoring wind turbines. Dzieciech et al.¹⁵ developed Instantaneous Circular Path Cycle Map (ICPCM)-based envelope analysis and time-synchronous averaging analysis for epicyclic gearbox fault detection. The ICPCM method consumes substantial computing resources. Although envelope analysis is a relatively effective way to detect and diagnose epicyclic gearbox faults, random noise is an unavoidable challenge when applying it for fault detection and diagnosis. Envelope analysis is the mainstream technology in processing the vibration signals of rotating machines. However, envelope analysis has shortages of noise inclusions¹⁶ and complex spectrum profiles which make it difficult to separate fault components and achieve an accurate diagnosis, especially for the data with low SNR due to incipient defects in planet, long vibration transmission paths, and variable operating conditions. The vibration signal from an epicyclic gear system in a commercial helicopter was investigated via envelope analysis by Elasha1 et al.¹⁷ and Zhou et al.¹⁸. A comprehensive literature review was given by Lei¹⁹ from the perspectives of modelling and analysing. The difficulties of fault detection and diagnosis desire more advanced sensing and processing methods. Fan and Li²⁰ installed a commercial accelerometer on the planet carrier using a slip ring to detect and diagnose planet bearing faults. The novel implementation can avoid the complex transmission path, but this method needs a significant modification on epicyclic gearboxes. Then, cepstrum whitening, minimum entropy deconvolution (MED), spectral kurtosis (SK), and envelope analysis are used to develop a logic detection and diagnosis routine.

In this paper, aiming to minimise the effect of varying transmission paths, On-Rotor Sensing (ORS) is employed to capture rotor vibrations. The modulation mechanism in ORS vibrations is analytically characterised to show the differences with conventional on-housing vibrations. The noise influence in envelope analysis is given in this paper. The noise and rich components in the squared envelope prevent effective fault diagnosis of epicyclic gearboxes. To further enhance equally spaced modulation harmonics in the squared envelope, Modulation Signal Bispectrum is employed to extract the equally spaced harmonics for effective fault diagnosis of compound faults of epicyclic gearboxes in the experimental study. The theoretical background including characteristic frequencies of epicyclic gearboxes, noise envelope properties and MSB method, is described in the Theoretical Background section. The experimental studies of data sensing and signal processing are given in the Gear Fault Diagnostics in an Epicyclic Gearbox section. Finally, the conclusions are drawn in the Final section.

Theoretical background

Epicyclic gearbox vibration characteristics with faults

A typical epicyclic gear set has a ring gear, several planet gears and a sun gear. If the ring gear is standstill, the planet gears rotate around the unfixed centres and mesh with the ring gear and sun gear simultaneously. The planet gears not only rotate around the moving centres but also revolve around the sun gear. The meshing stiffness varies significantly along with the number of meshing teeth during the gear train rotation and consequently, gear meshing vibrations are rich in periodic components. Several planet gears are meshing simultaneously with the sun gear and the ring gear, and a large number of similarly periodic components could exist in the vibration of epicyclic gearboxes. These same periodic vibrations with different meshing phases are coupled with each other.⁵ In addition, the vibration responses are transmitted to on-housing accelerometers through multiple and time-varying transmission paths. These complex transmission paths attenuate the desired fault information,¹⁹ and additionally, large quantities of background noise are added into the vibration signals, which is the most challenging problem in the fault diagnosis of epicyclic gearboxes.

Fault characteristic frequencies of epicyclic gearboxes. To introduce the characteristic frequencies of the epicyclic gearbox, the corresponding nomenclature is defined here. In this paper, Z_R , Z_P and Z_S are the tooth number of the ring gear, planet gear and sun gear.

K denotes the number of planet gears. f_{rc} , f_{rp} and f_{rs} are the rotating frequency of the carrier, the planet gear and the sun gear, respectively.

The meshing between the planet gear, the sun gear and the ring gear determines that the passing tooth number in rotation is the same, and thereafter, the meshing frequency of the planet gear and the ring gear is the same as that of the sun gear and the planet gear. f_M is the meshing frequency of the epicyclic gearbox. The rotation frequency of the shaft connected with the sun gear is known as f_{rs} , and the meshing frequency can be calculated as

$$f_M = \frac{Z_R Z_S}{Z_R + Z_S} f_{rs} = Z_R f_{rc} \quad (1)$$

A localised tooth defect on the gears results in periodic impulses, which are modulated by the meshing frequencies and natural frequencies of the gearbox. If the localised fault occurs on the sun gear, the vibration responses become pronounced when the fault meshes with a planet gear and then go back to a normal condition when the fault runs out the meshing area. With the rotating of the sun gear, the fault meets K planet gears consecutively. Assume that the impacts between the fault on the sun gear and the planet gears are identical. The characteristic fault frequency of the sun gear is

$$f_{sf} = K \frac{f_M}{Z_S} = K \frac{Z_R}{Z_R + Z_S} f_{rs} \quad (2)$$

The identical impacts induced by faults are a hypothesis, and due to the manufacture and installation errors, the localised defect induced impacts are varying especially under nonstationary working conditions. Therefore, the non-integer ($i/K \notin N^+$) harmonics are also visible in the vibration spectrum.

Similarly, when the planet gear has a localised defect, the collisions induced by the defect would happen twice with the sun gear and the ring gear in one revolution. Hence, the characteristic fault frequency of the planet gear is expressed as

$$f_{pf} = 2 \frac{f_M}{Z_P} = 2 \frac{Z_R Z_S}{Z_P (Z_R + Z_S)} f_{rs} \quad (3)$$

Vibration signal model of faulty gear meshing. The faults on planet and sun gears result in an AM/PM effect to the gear meshing vibration.⁴ The main difference is that two faults generate different characteristic frequencies. If the transmission path is not inclusive, the modulation signals of gear meshing can be simulated as an AM/PM signal. The meshing frequency of gear pairs is the carrier and the fault characteristic frequency is the modulating signal. Therefore, the modulation signal of the vibration can be expressed as

$$s(t) = \sum_{i=1}^I [C_i + a(t)] \cos[2\pi i f_{mesh} t + b(t) + \varphi_i] \quad (4)$$

with

$$\begin{cases} a(t) = \sum_{m=1}^M A_m \cos(2\pi m f_{\text{fault}} t + \alpha_m) \\ b(t) = \sum_{n=1}^N B_n \sin(2\pi n f_{\text{fault}} t + \beta_n) \\ c_i(t) = C_i \cos(2\pi i f_{\text{mesh}} + \varphi_i) \end{cases} \quad (5)$$

in which $a(t)$ and $b(t)$ represent the AM and PM effects due to the localised gear fault on either planet gear or sun gear. A_m and α_m are the amplitude and phase of the amplitude modulating signals. B_n is the amplitude of the phase modulating signals, of which the phase is denoted by β_n . $C_i(t)$ is the i_{th} order meshing signal. C_i and φ_i denote the amplitude and phase of i_{th} order meshing signal. Without losing generality, it is simplified that only the fundamental characteristic frequency of the damaged gear and the gear meshing frequency is considered in the following contents. Consequently, the vibration signal model of a faulty gear pair yields

$$s(t) = [C_i + A \cos(2\pi f_{\text{fault}} t + \alpha)] \cos[2\pi f_{\text{mesh}} t + B \sin(2\pi f_{\text{fault}} t + \beta) + \varphi] \quad (6)$$

The model can be expanded using the Jacobi–Anger expansion, which can be expressed as

$$s(t) = [C_i + A \cos(2\pi f_{\text{fault}} t + \alpha)] \sum_{K=-\infty}^{\infty} J_k(B) \cos[2\pi (f_{\text{mesh}} + k f_{\text{fault}}) t + k\beta + \varphi] \quad (7)$$

where $J_k(B)$ is the Bessel function of the first kind at the integer order k with the argument B . Equation (7) can be further simplified using trigonometric functions and it is shown as follows

$$\begin{aligned} s(t) = & C_i \sum_{K=-\infty}^{\infty} J_k(B) \cos[2\pi (f_{\text{mesh}} + k f_{\text{fault}}) t + k\beta + \varphi] \\ & + \frac{A}{2} \sum_{K=-\infty}^{\infty} J_k(B) \cos[2\pi (f_{\text{mesh}} + (k+1) f_{\text{fault}}) t + k\beta + \varphi + \alpha] \\ & + \frac{A}{2} \sum_{K=-\infty}^{\infty} J_k(B) \cos[2\pi (f_{\text{mesh}} + (k-1) f_{\text{fault}}) t + k\beta + \varphi - \alpha] \end{aligned} \quad (8)$$

It can be seen from equation (8) that the vibration signal from a faulty gear pair has numerous sidebands around the meshing frequency f_{mesh} . Furthermore, the sidebands are equally spaced with the gap of the characteristic fault frequency f_{fault} . However, this signal model is not inclusive of the transmission path effects. In most circumstances, ring gears of epicyclic gearboxes are stationary, which is also the considered case in this paper. Usually, the conventional accelerometer is installed on the gearbox housing to acquire

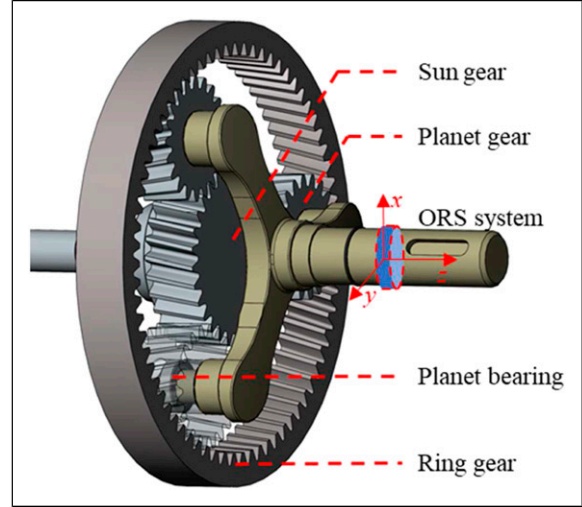


Figure 1. ORS sensor on an epicyclic gear set.

the vibration responses from the gear meshing. If the manufacture errors and installation errors are omitted, the transmission paths of the sun-planet gear meshing and the planet-ring gear meshing are varying due to the rotation of the sun gear and the planet gear. Furthermore, the rotation of the planet gear is around unfixed centres. These complicated transmission paths can deteriorate the quality of the vibration signal from the faulty gears due to dissipation and interference.¹⁹ The conventional method is difficult to extract the weak features due to the contamination of the noise and the impacts from nearby machines or components. The conventional on-shell accelerometer is challenging to isolate the desired information. To overcome this bottleneck problem, the On-Rotor Sensing (ORS) technique²¹ is developed to directly obtain the rotor vibration signals.

Figure 1 shows a schematic diagram of the ORS sensor installed on an epicyclic gear set. The ORS accelerometer is directly attached to the carrier rotor and rotates with the carrier simultaneously.

Imaging that the gears and bearings are isotropic, the planet gear fault induced AM/PM vibration signals can be directly captured by the tri-axis ORS accelerometer. The localised fault on the planet gear has a fixed angle with the three axes of the ORS accelerometer when meshing with the sun gear or ring gear. Owing to the fixed transmission path, no additional modulation is involved and consequently, the planet gear fault induced AM/PM vibration of ORS measurements can be expressed by equation (6), which then can be expanded into a sum of multiple components by equation (8).

To be different, the relative speed between the sun gear and planet gear inevitably results in additional modulation. The relative movement results in a varying angle between the impacts and the sensor axis. The projection of the vibration onto the sensor axis introduces the additional modulation effect, which can be modelled using a Hanning

window.^{2,3} The ORS vibration of the sun gear fault can be expressed by

$$s(t) = \underbrace{[1 - \cos(2\pi(f_{rs} - f_{rc})t)]}_{\text{Additional AM}} [C + A \cos(2\pi f_{\text{fault}}t + \alpha)] \cos[2\pi f_{\text{mesh}}t + B \sin(2\pi f_{\text{fault}}t + \beta) + \varphi] \quad (9)$$

For the sun gear fault, the characteristic sun fault frequency is $f_{\text{fault}} = f_{rs} - f_{rc}$. Therefore, the sun gear fault induced AM/PM vibration of ORS measurements yields

$$s(t) = [1 - \cos(2\pi f_{\text{fault}}t)] [C + A \cos(2\pi f_{\text{fault}}t + \alpha)] \cos[2\pi f_{\text{mesh}}t + B \sin(2\pi f_{\text{fault}}t + \beta) + \varphi] \quad (10)$$

It can be seen that the additional modulation is also related to the characteristic fault frequency of the sun gear. The additional modulation can be avoided if installing another ORS sensor on the shaft connected to the sun gear. To make the condition monitoring cost-effective, only one ORS sensor is installed on the carrier shaft. The modulation signal of ORS measurements for the sun gear fault case can be expanded into a sum of multiple components, which is expressed as follows

$$\begin{aligned} s(t) = & C \sum_{K=-\infty}^{\infty} J_k(B) \cos[2\pi(f_{\text{mesh}} + kf_{\text{fault}})t + k\beta + \varphi] \\ & + \frac{A}{2} \sum_{K=-\infty}^{\infty} J_k(B) \cos[2\pi(f_{\text{mesh}} + (k+1)f_{\text{fault}})t + k\beta + \varphi + \alpha] \\ & + \frac{A}{2} \sum_{K=-\infty}^{\infty} J_k(B) \cos[2\pi(f_{\text{mesh}} + (k-1)f_{\text{fault}})t + k\beta + \varphi - \alpha] \\ & - \frac{C}{2} \sum_{K=-\infty}^{\infty} J_k(B) \cos[2\pi(f_{\text{mesh}} + (k-1)f_{\text{fault}})t + k\beta + \varphi] \\ & - \frac{C}{2} \sum_{K=-\infty}^{\infty} J_k(B) \cos[2\pi(f_{\text{mesh}} + (k+1)f_{\text{fault}})t + k\beta + \varphi] \\ & - \frac{A}{4} \sum_{K=-\infty}^{\infty} J_k(B) \cos[2\pi(f_{\text{mesh}} + f_{\text{fault}})t + k\beta + \varphi + \alpha] \\ & - \frac{A}{4} \sum_{K=-\infty}^{\infty} J_k(B) \cos[2\pi(f_{\text{mesh}} + (k+2)f_{\text{fault}})t + k\beta + \varphi + \alpha] \\ & - \frac{A}{4} \sum_{K=-\infty}^{\infty} J_k(B) \cos[2\pi(f_{\text{mesh}} + (k-2)f_{\text{fault}})t + k\beta + \varphi - \alpha] \\ & - \frac{A}{4} \sum_{K=-\infty}^{\infty} J_k(B) \cos[2\pi(f_{\text{mesh}} + f_{\text{fault}})t + k\beta + \varphi - \alpha] \end{aligned} \quad (11)$$

It can be observed from both faulty cases of planet and sun gears by equations (8) and (11) that the ORS measurements from malfunction epicyclic gearboxes are rich in multiple components around the meshing frequencies. These equations are an ideal condition for perfect epicyclic gearboxes under stable working conditions. However, the manufacture and installation errors, as well as transiently unstable working conditions, lead to random phase variation

and additional discrete components, making the fault detection and diagnosis more challenging and in addition, strong background noise increases the difficulty further. To restrain the random phase variation, the squared envelope analysis is used to characterise second order cyclostationary ORS vibrations.

Noise and multiple components in envelope analysis

Squared envelope. The envelope of a random signal was defined by Rice in reference 22, which is described as follows. Assume that the signal is

$$s(t) = \sum_{k=0}^{\infty} A_k \cos(\omega_k t + \phi_k) \quad (12)$$

where A_k is the amplitude and ϕ_k are the mutually independent phases. The amplitude A_k yields to

$$\sum_{k=0}^{\infty} A_k = \int s(\omega) d\omega \quad (13)$$

where $s(\omega)$ is the power spectrum of the signal $s(t)$. Let $\bar{\omega}$ be the mid-band frequency in this power spectrum, the signal can be rewritten as

$$s(t) = \Re\left(A(t)e^{i\bar{\omega}t}\right) \quad (14)$$

in which

$$A(t) = \sum_{k=0}^{\infty} A_k \exp\left[i(\omega_k - \bar{\omega})t + \phi_k\right] = s_e(t)e^{i\Phi(t)} \quad (15)$$

Here, (t) is the real envelope²² and it can be easily obtained by

$$s_e(t) = \sqrt{\left\{ \sum_{k=0}^{\infty} A_k \cos(\omega_k t + \phi_k) \right\}^2 + \left\{ \sum_{k=0}^{\infty} A_k \sin(\omega_k t + \phi_k) \right\}^2} \quad (16)$$

The envelope of the signal can be obtained easily based on the Hilbert transform, which alters the phase of every component by $\pi/2$. The analytic signal (t) can be expressed as

$$s_a(t) = s(t) + iH(s(t)) \quad (17)$$

in which $H(\cdot)$ denotes the Hilbert transform of the time domain signal. Both the real and imaginary parts yield to a normal distribution if the signal $s(t)$ is normally distributed, centred at zero, and independent. The absolute values of the analytic signals are the envelope or named as the instantaneous amplitude.

Envelope analysis is prevalent in fault detection and diagnosis of rolling element bearings and it has been demonstrated that envelope analysis is powerful to characterise

cyclostationary signals. The effectiveness of the envelope analysis is owing to that the envelope detects the energy oscillation of the signals. The envelope yields spurious high-order harmonics in the spectrum due to the inevitable aliasing problem, whilst the squared envelope can prevent producing sharp to avoid the possible aliasing.²³ The squared envelope has more merits because it has a strong connection with another effective approach, spectral correlation, for analysing the cyclostationary signals.²³ The relationship between squared envelope and spectral correlation is described in the following contents. The spectral correlation is defined as

$$S(\alpha, f) = \iint E \left[x \left(t + \frac{\tau}{2} \right) x^* \left(t - \frac{\tau}{2} \right) \right] e^{-i2\pi\alpha t} e^{-i2\pi f \tau} dt d\tau \quad (18)$$

The spectral correlation results have the cyclic frequency and normal frequency axis and the integral of the spectral correlation along the normal frequency axis leads to a discrete spectrum of the cyclic frequency axis,²⁴ yielding

$$\begin{aligned} \int S(\alpha, f) df &= \iint E \left[x \left(t + \frac{\tau}{2} \right) x^* \left(t - \frac{\tau}{2} \right) \right] e^{-i2\pi\alpha t} \left(\int e^{-i2\pi f \tau} df \right) dt d\tau \\ &= \iint E \left[x \left(t + \frac{\tau}{2} \right) x^* \left(t - \frac{\tau}{2} \right) \right] \delta(\tau) e^{-i2\pi\alpha t} dt d\tau \\ &= \int E [x(t)x^*(t)] e^{-i2\pi\alpha t} dt \\ &= \int E [x^2(t)] e^{-i2\pi\alpha t} dt \end{aligned} \quad (19)$$

The integral of the spectral correlation over normal frequency is equivalent to the spectrum of the squared signal. However, the squared operation of real signals inevitably brings additional components due to the aliasing effects.²³ In contrast, the squared operation can be achieved by the analytic signal multiplying with its complex conjugate, which is also called squared envelope. The squared envelope can be expressed as

$$s_{se}(t) = s_a(t)s_a^*(t) \quad (20)$$

The squared envelope does not involve the additional components but the desired diagnostic information only. Therefore, the squared envelope often serves as an effective method to characterise the cyclostationary signals. However, vibration signals acquired from a running machine is always subjected to random noise interference. The calculation of squared envelope by such methods inevitably includes noise influences, resulting in inaccurate demodulation results.

Noise in envelope analysis. The linear property of the Hilbert transform allows a linear representation of the analytic signal. Assume that the original $n(t)$ is an uncorrelated normally distributed noise with a standard deviation σ and

zero mean. Envelope $n_e(t)$ of the noise $n(t)$ obeys the Rayleigh distribution²⁵ as

$$f(x; \sigma) = \frac{x}{\sigma^2} e^{-\frac{x^2}{2\sigma^2}}, x \geq 0 \quad (21)$$

The example of the noise signal and its envelope is shown in Figure 2(a) and the probability density functions (PDFs) of the noise signal and the envelope signal are depicted in Figure 2(b). The noise itself obeys the normal distribution and the envelope obeys the Rayleigh distribution.

The statistical characteristics^{25,26} of the squared envelope $n_e^2(t)$ can be summarised as follows

$$E(n_e^2(t)) = 2C_n(0) \quad (22)$$

$$D(n_e^2(t)) = 4C_n(0)^2 \quad (23)$$

$$S_{n_e^2}(\omega) = 8 \int_0^\infty S_n(\sigma) S_n(\sigma + \omega) d\sigma \quad (24)$$

$E(\)$ and $D(\)$ denote the mean value and the variance; $C_n(\tau)$ is the autocovariance of $n(t)$; $S_n(\omega)$ is the power spectrum of the $n(t)$; $C_{n_e}(\tau)$ is the autocovariance of the $n_e(t)$ and $S_{n_e}(\omega)$ is the power spectrum of the $n_e(t)$.

Moreover, the envelope $n_e(t)$ is a bit complicated than the squared envelope. The mean value and variance of the envelope are expressed by equations (25) and (26). The power spectrum of the envelope can be estimated by equation (27). The first item dominates the spectra contents of the envelope spectra and it tells that the white noise in the envelope does not obey the normal distribution. The energy of the whole envelope signal is more concentrated in the low-frequency range. The negative and positive frequencies of the envelope in the frequency domain are shifted towards each other. The noise in the envelope is no longer white and the negative effects of the noise are not suppressed, which influences the robustness and accuracy of the fault diagnosis

$$E(n_e(t)) = \sqrt{\frac{\pi}{2}} C_n(0) = 1.253 \sqrt{C_n(0)} \quad (25)$$

$$D(n_e(t)) = \left(2 - \frac{\pi}{2} \right) C_n(0) = 0.429 C_n(0) \quad (26)$$

$$\begin{aligned} S_{n_e^2}(\omega) &= \frac{\pi}{4C_n(0)} \int_0^\infty S_n(\sigma) S_n(\sigma + \omega) d\sigma \\ &+ \frac{1}{64C_n(0)^3} \int_0^\infty \rho(\tau)^4 \cos(\omega\tau) d\tau \\ &+ \frac{1}{256C_n(0)^5} \int_0^\infty \rho(\tau)^6 \cos(\omega\tau) d\tau + \dots \end{aligned} \quad (27)$$

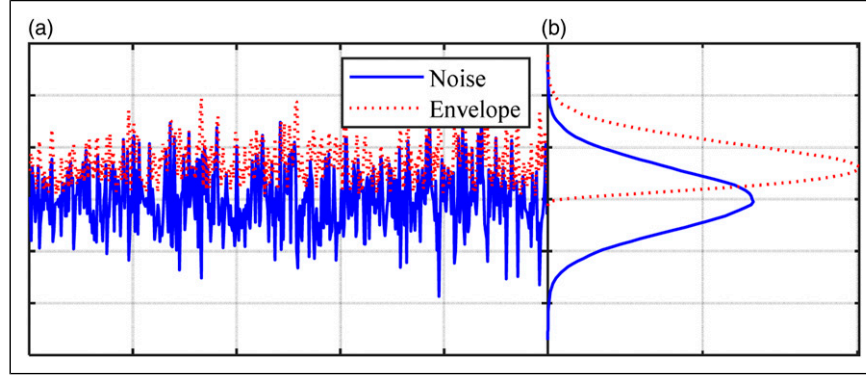


Figure 2. PDFs of the random noise and its envelope.

where

$$\rho(\tau) = \sqrt{[\int_0^\infty S_n(\omega)\cos(\omega\tau)d\omega]^2 + [\int_0^\infty S_n(\omega)\sin(\omega\tau)d\omega]^2}.$$

It can be seen that the noise still presents in the envelope signal but the normal distribution change to the Rayleigh distribution. The noise deteriorates the desired fault signatures, and therefore, noise reduction is required to extract accurate fault features.

Multiple harmonics in the envelope. It can be seen from equations (8) and (11) that there are numerous sidebands around meshing frequency in gear vibrations. The squared envelope can obtain the envelope signal that contains plentiful harmonics of the fault frequency. However, the demodulation process inevitably involves other components that are not related to the gear faults. The epicyclic gear faults can induce numerous harmonics in the squared envelope signal which can be expressed as

$$s_{se}(t) = \sum_{i=1}^{\infty} \Re(A_i e^{2\pi i f_{fault} t + \phi_i}) + n_{se}(t) \quad (28)$$

where $n_{se}(t)$ represents the noise and the other irregular discrete components. The equally spaced harmonics can be extracted to enhance the fault signatures. To reduce background noise and extract sparse harmonics, the Modulation Signal Bispectrum (MSB) method is employed to enhance the squared envelope results. The properties of the squared envelope denote that the noise in the original signals cannot be suppressed effectively, which leads to the ineffectiveness of the squared envelope in the early fault detection and diagnosis of epicyclic gearboxes. MSB has been investigated in references 27–31 to extract the modulating components in the vibration, acoustic and motor current signals for detecting and diagnosing faults in a wide range of mechanical and electrical machines. It has been verified that the MSB is highly effective in extracting incipient fault signatures from monitored data.³² The definition of MSB is

$$B_{MS}(f_1, f_2) = E[X(f_1 + f_2)X(f_1 - f_2)X^*(f_1)X^*(f_2)] \quad (29)$$

where $X(f) = \int_{-\infty}^{+\infty} x(t)e^{-i2\pi ft}$ denotes the Fourier transform of a temporal signal $x(t)$; f_1 and f_2 are two frequency components in the frequency domain signal; $X^*(f_1)$ is the complex conjugate of $X(f_1)$ and $E[\]$ denotes the expectation operator. For a perfect periodically modulated signal, the phase of the MSB can be calculated as

$$\phi(f_1, f_2) = \phi(f_1 + f_2) + \phi(f_1 - f_2) - \phi(f_1) - \phi(f_2) \quad (30)$$

with

$$\begin{cases} \phi(f_1 + f_2) = \phi(f_1) + \phi(f_2) \\ \phi(f_1 - f_2) = \begin{cases} \phi(f_1) - \phi(f_2), AM \\ \phi(f_1) - \phi(f_2) + \pi, PM \end{cases} \end{cases} \quad (31)$$

The phase of $X(f_1 + f_2)X(f_1 - f_2)X^*(f_1)X^*(f_2)$ of the coupled components is constant. This means that MSB of different signal segments can be averaged to enhance modulation characteristics. At the same time, this averaging operation suppresses background noise and non-modulation components due to their random phases. The MSB method can generate an optimal result for stationary signals with discrete frequency components, which is fictitious in machine vibration signals. Cyclostationary signals are practical in vibration-based machine condition monitoring. Therefore, the squared envelope is employed to extract the cyclic variation and then the first order cyclic features are further enhanced by the MSB method with regards to noise reduction and sparse representation. Any three harmonics with equal intervals are equivalent to a modulation signal and can be extracted by MSB as a sparse representation. There are any three components with equal interval mf_{fault} , which is expressed as

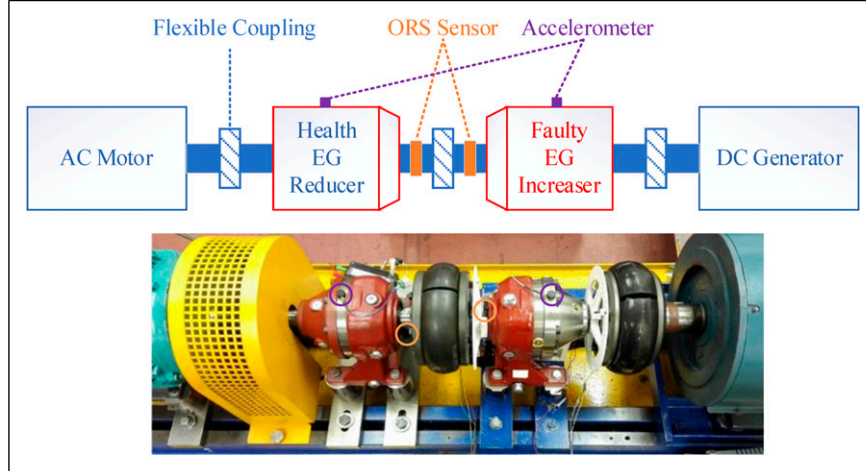


Figure 3. Schematic diagram and photograph of the epicyclic gearbox test rig.

$$\begin{aligned}
 s_{se}(t) = & \Re(A_{n-m}e^{2\pi(n-m)f_{fault}t+\phi_{n-m}}) \\
 & + \Re(A_n e^{2\pi n f_{fault}t+\phi_n}) \\
 & + \Re(A_{n+m}e^{2\pi(n+m)f_{fault}t+\phi_{n+m}}) + n_{se}(t)
 \end{aligned} \quad (32)$$

The phase of $X(f_1 + f_2)X(f_1 - f_2)X^*(f_1)X^*(f_1)$ is $\phi_{n-m} + \phi_{n+m} - 2\phi_n$ and hence a peak at (nf_{fault}, mf_{fault}) shows on the bispectrum plane. Therefore, MSB Enhanced Squared Envelope can enhance the equally spaced harmonics associated with epicyclic gear faults. The three-dimensional MSB results require a certain degree of expertise, a more succinct illustration, MSB enhanced envelope spectrum, is used to make the high-order spectrum more interpretable and comparable. The MSB Enhanced Squared Envelope spectrum (MSB-ESE) can be concentrated via the integral of the complex MSB magnitudes along the carrier frequency direction, which can be expressed as

$$F_e(f_2) = \int_{f_{low}}^{f_{high}} B_{MS}(f_1, f_2) df_1 \quad 33$$

in which f_{low} and f_{high} are the frequency range of f_1 in the MSB calculation. The integral of the MSB magnitudes along the carrier frequency axis can focus on the modulation components and suppress the other uncorrelated components.

Gear fault diagnostics in an epicyclic gearbox

ORS measurements from an epicyclic gearbox test rig

The experimental studies were conducted to demonstrate the effectiveness of the MSB Enhanced Squared Envelope approach. The schematic diagram and photograph of the epicyclic gearbox test rig are shown in Figure 3. Two back-to-back 10 kW epicyclic gearboxes are connected by the

flexible couplings as the speed reducer and increaser, respectively in the transmission line. The power source of the test rig comes from an induction motor and is consumed by the DC generator.

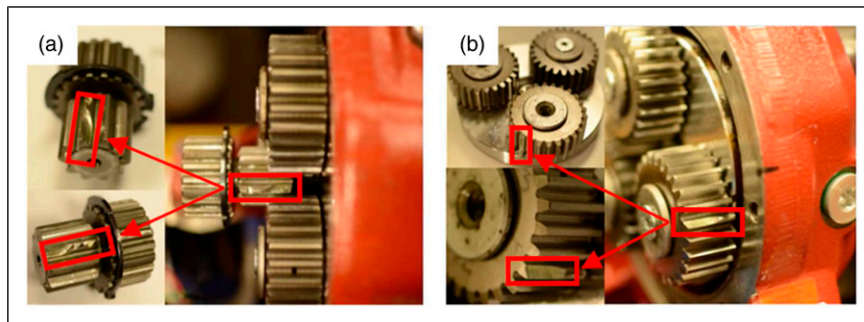
The configuration of these two epicyclic gearboxes has slight differences for the purpose of minimising mutual interference of the vibration signals from each epicyclic gearbox. The key specifications of the test rig are shown in Table 1.

One of the epicyclic gearboxes is healthy and it is considered as the baseline in the experimental studies and the other one has compound defects on the sun gear and planet gear, respectively. The photographs of the gear faults are shown in Figure 4. Figure 4(a) shows that the fault on the sun gear is simulated by removing around 60% of the gear tooth face along the width and Figure 4(b) depicts the planet gear defect is seeded by milling about 60% of the tooth face.

The developed ORS sensors are installed on the output and input rotating shaft of the health and faulty epicyclic gearbox, respectively. The ORS sensors are rotating along with the carrier and consequently the ORS sensor has a fixed angle to the defect planet gear and therefore, the impacts induced by the localised defects have an identical transmission path, which is an advantage compared to the conventional on-housing vibration. The key specifications of the used ORS sensors are listed in Table 1. During the epicyclic gearbox tests, two ORS sensors were configured to operate within a dynamic range of ± 16 g at a sampling frequency of 1600 Hz. The test rig was operated at 40% and 60% of the full motor speed and three different load conditions (50%, 75% and 90% of the full load). The ORS vibration signals were logged for 60 s at each working condition. The acquired signals were saved into a local storage card as comma-separated value (CSV) files, and then to be read and processed after tests. Two on-housing accelerometers were installed on each epicyclic gearbox and

Table 1. Key specifications of the epicyclic gearbox test rig.

Test rig components		Key specifications
Induction motor		11 kW, full speed 1500 r/min
DC generator		85 kW, full speed 1850 r/min
Baseline epicyclic gearbox	Sun gear	13 teeth
	Planet gear	24 teeth, 4 gears
	Ring gear	62 teeth
Faulty epicyclic gearbox	Sun gear	10 teeth
	Planet gear	26 teeth, 3 gears
	Ring gear	62 teeth
ORS sensor	Accelerometer	ADXL345, 1600 Hz, 16g
	Processor	nRF52840, Cortex-M4F, BLE5.0

**Figure 4.** Photographs of gear faults (a) sun gear fault (b) planet gear fault.**Table 2.** Fault characteristic frequencies of the faulty sun and planet gears.

Rotating speed	f_{rc}	f_{rp}	f_{rs}	f_M	f_{sf}	f_{pf}
40%	1.80 Hz	2.49 Hz	12.94 Hz	111.41 Hz	33.42 Hz	8.57 Hz
60%	2.69 Hz	3.73 Hz	19.38 Hz	166.92 Hz	50.07 Hz	12.84 Hz

on-housing vibration signals are collected for 30 s at a sampling rate of 25 kHz at each test condition. The rotating frequencies and characteristic fault frequencies of the planet and sun gears in the faulty epicyclic gearbox are listed in [Table 2](#).

Conventional squared envelope analysis

As introduced in the description of the experiments, ORS signals represent the vibration of the rotors. The MEMS accelerometers are collecting the absolute accelerations and consequently, the main component of the ORS vibrations is the alternation of gravity along with the rotation of the shaft. The results of envelope and MSB-ESE used the ORS vibrations at speed 60% and load 90% as an example to explain. The MSB-ESE results at other working conditions are provided in the [Appendix 1](#). [Figures 5\(a\) and \(c\)](#) display the temporal ORS vibrations from the faulty and baseline epicyclic gearboxes, respectively, and the most pronounced

cycle in the time domain signal is the carrier shaft rotating frequency. The ORS vibrations from the faulty gearbox have a higher amplitude. As shown in [Figure 5\(b\) and \(d\)](#), the spectra of the time domain signals are obtained by the Fourier transform. The most pronounced component in the amplitude spectra is the rotating frequency of the carrier. In addition, the spectrum of the faulty gearbox contains more discrete components and these components are higher than that in the baseline spectrum.

Based on the outline of the spectrum, two frequency bands are selected to extract the fault information. The frequency band from 100 Hz to 500 Hz is selected as the low-frequency band because most of the obvious elements are included in this range. The high-frequency band is selected from 500 Hz to 700 Hz, which does not have pronounced elements but is potentially rich in fault information owing to the significant modulation phenomenon. Then, two bandpass filters were designed to obtain the low-frequency band signal and high band frequency signal. The squared envelopes of the low and

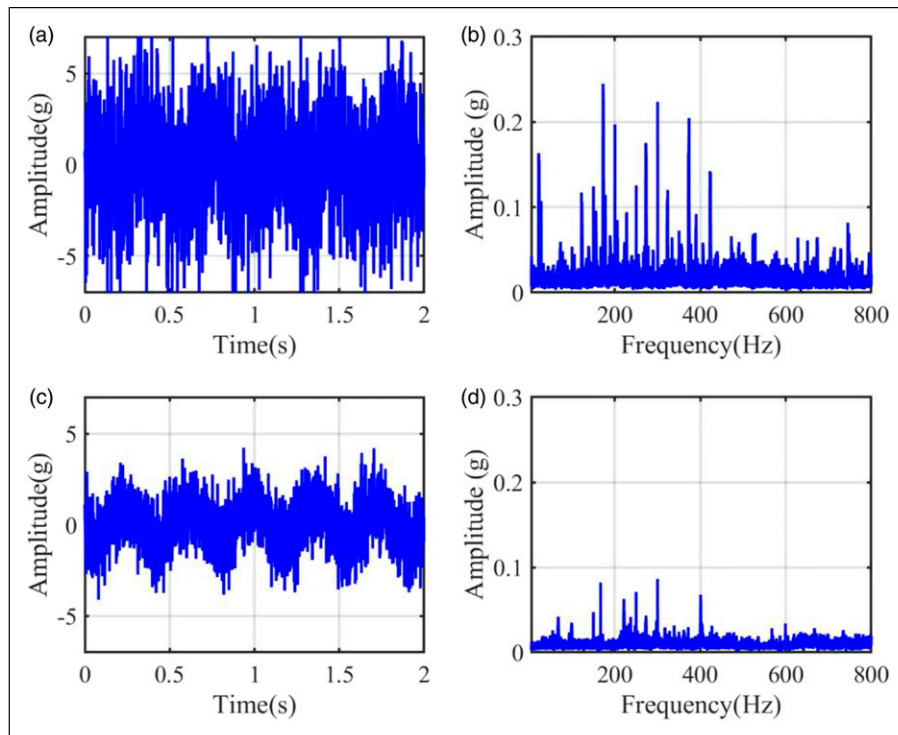


Figure 5. ORS vibrations from two epicyclic gearboxes: (a) temporal signals from the faulty gearbox; (b) spectrum of (a); (c) temporal signals from the baseline gearbox and (d) spectrum of (c).

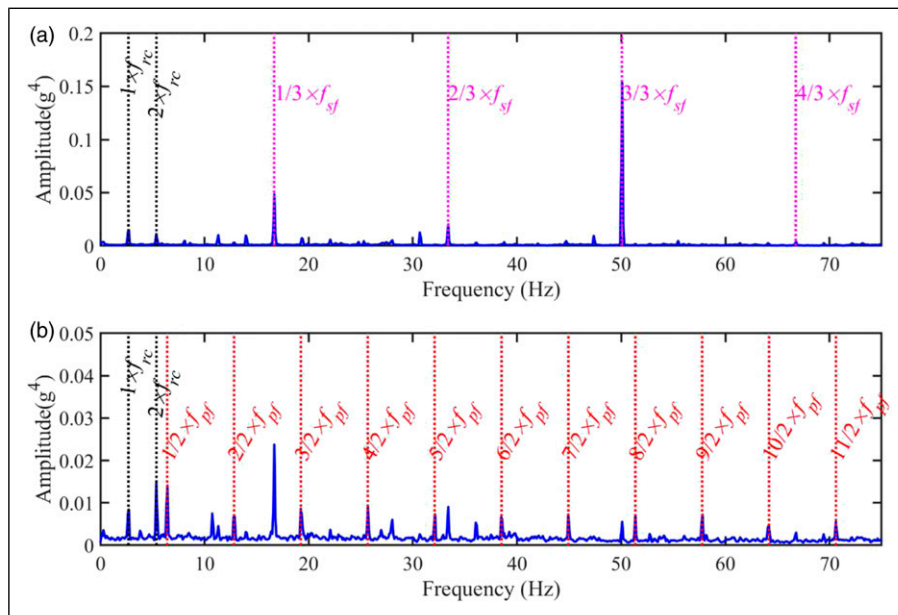


Figure 6. Envelope spectra of ORS vibrations for faulty case: (a) in the low-frequency band and (b) in the high-frequency band.

high-frequency bands can be obtained by the construction of analytic signals from two orthogonal ORS outputs. Figure 6 and Figure 7 display the squared envelope spectra of the ORS vibrations from the faulty and baseline epicyclic gearboxes,

respectively. Figure 6(a) and (b) show the squared envelope spectra of the low and high-frequency band signals of the faulty case, respectively. The envelope spectrum is an ensemble average of the amplitude spectra from the segmented

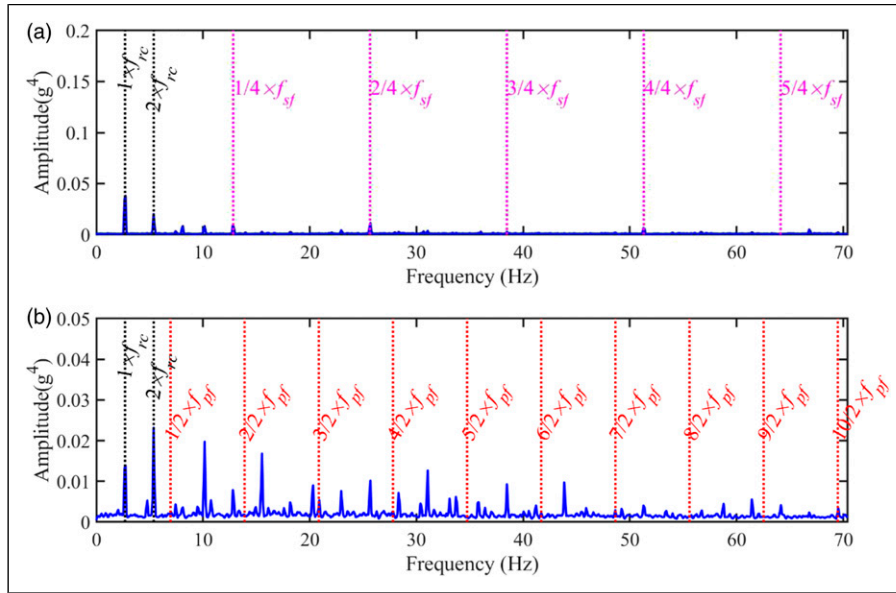


Figure 7. Envelope spectrums of ORS vibrations for baseline case: (a) in the low-frequency band and (b) in the high-frequency band.

squared envelope signals. The ensemble average increases the reliability and accuracy of the envelope analysis. The segment length in the calculation is selected as 16,384, which gives a frequency resolution of 0.1 Hz. The fine frequency resolution allows distinguishing the characteristic frequencies. The overlap ratio between segments is set as 0.7, which increases the average times for a better representation of the final result. These parameters allow 20 times average for the displayed envelope spectra. It is obvious that the compound faults can be detected in these two envelope spectra, which demonstrates the effectiveness of the ORS technique. As the faulty gearbox has three planet gears, the sub-harmonics of the characteristic sun gear fault frequency are also manifest in Figure 6(a). The characteristic frequency of the sun gear fault is dominating in the low-frequency band envelope spectrum. The envelope spectrum of the high-frequency band signal in Figure 6(b) shows that the multiple harmonics and sub-harmonics of the characteristic planet gear fault frequency are pronounced. The envelope spectra of the baseline case in Figure 7 show that the characteristic fault frequencies are nearly invisible.

MSB Enhanced Squared Envelope analysis

Through the envelope analysis, the sun gear faults can be diagnosed. However, the signature of the planet gear faults is not pronounced and the results are mixed with some other irrelevant components. To give a more convinced and reliable representation, the MSB enhanced envelope method is used to highlight the sun and planet gear fault features. In the MSB analysis, the segment length and the overlap ratio are set the same as that in the envelope analysis, leading to equal

average times. 20 times of average of MSB is not much in a noisy vibration signal analysis. A promising result of MSB relies on more average if the signal contains more random noise. Figure 8 and Figure 9 show the MSB magnitudes of the envelope from the faulty and baseline ORS measurements. As the aforementioned envelope analysis, squared envelope signals in the low-frequency band and high-frequency bands were obtained using Hilbert transform based on the manually selected two frequency bands. Two envelope signals are used as the input of the MSB method. Then the MSB results are presented in Figure 8(a) and (b), respectively. As can be observed, the fault signatures of the sun gear and planet gear can be further highlighted. The low noise carpet and strong fault features denote that the noise in the ORS vibrations is not too much because these results are obtained using only 20 times of average. For the baseline case in Figure 9, the MSB extracts some modulation components but these coupled components are not from the gear faults.

Figure 10 and Figure 11 depict the MSB-ESE of the faulty and baseline cases, respectively. As shown in Figure 10(a), the sub-harmonics of the characteristic sun gear fault frequency are pronounced, and the dominating component is the sun gear fault frequency. Figure 10(b) gives a much better diagnosis result than that of the envelope analysis. The sub-harmonics and harmonics of the characteristic planet gear fault frequency are highlighted in the MSB-ESE whilst the other uncorrelated components are significantly suppressed. To verify the diagnostic results, the MSB-ESE of the ORS vibrations from the baseline case is shown in Figure 11. The baseline epicyclic gearbox works in a smooth and good condition, and consequently, the characteristic fault

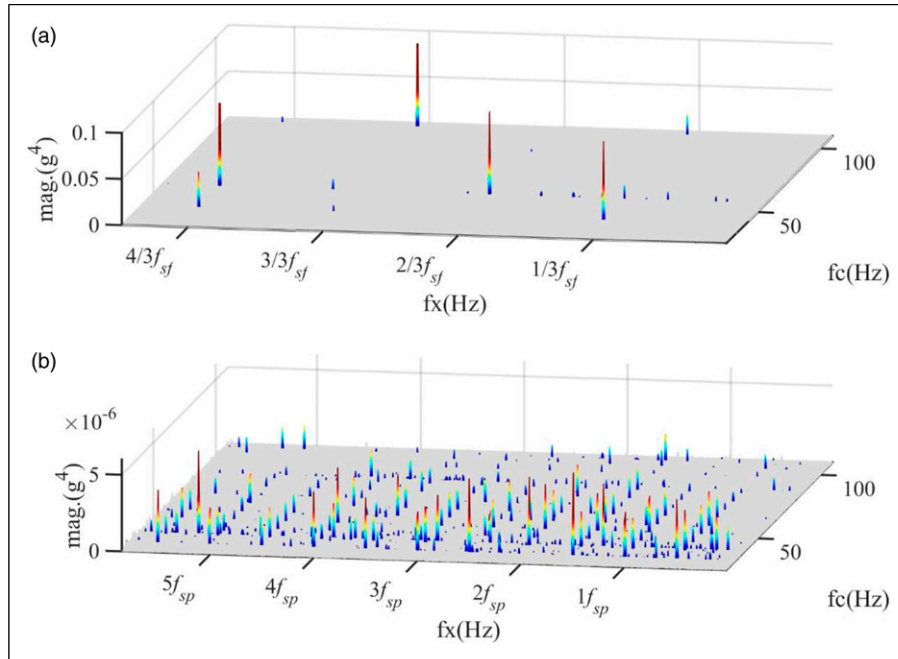


Figure 8. MSB-ESE of ORS vibrations for faulty case: (a) in the low-frequency band and (b) in the high-frequency band.

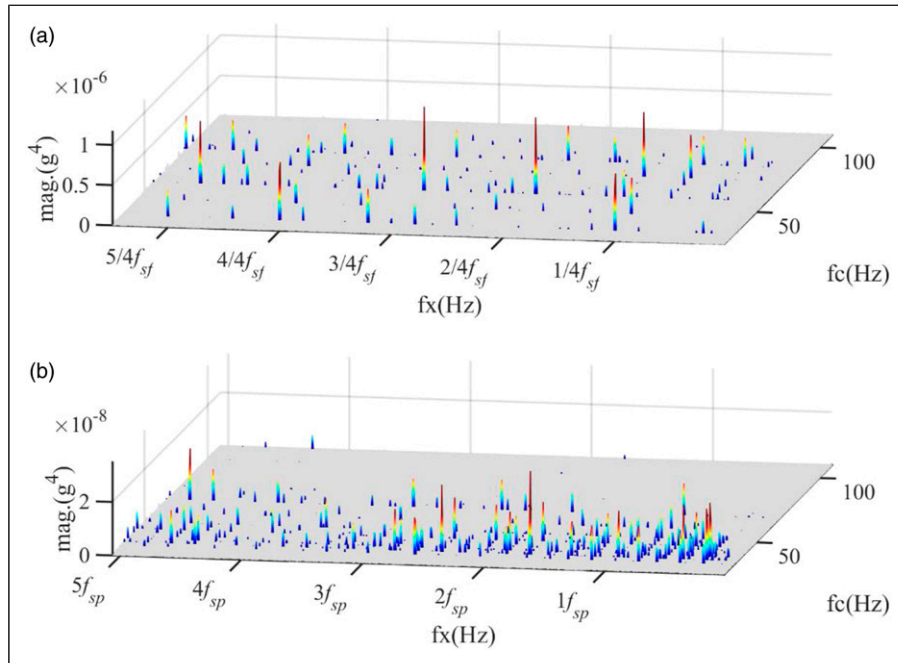


Figure 9. MSB-ESE of ORS vibrations for baseline case at 60% speed and 90% load: (a) in the low-frequency band and (b) in the high-frequency band.

frequencies are about 10 thousand smaller than the faulty one in the MSB-ESE (refer to the [Appendix 1](#) for more results at the other five working conditions).

To show the effectiveness of the proposed MSB-ESE, the spectra using on-housing vibrations are also calculated, which

is shown in [Figure 12](#). It can be seen that the proposed method is also effective to obtain the sun gear and planet gear fault features. However, due to the intricate modulation, the sidebands f_{rc} around the sun gear fault frequency f_{sf} are also obvious. This result shows the effectiveness of the proposed

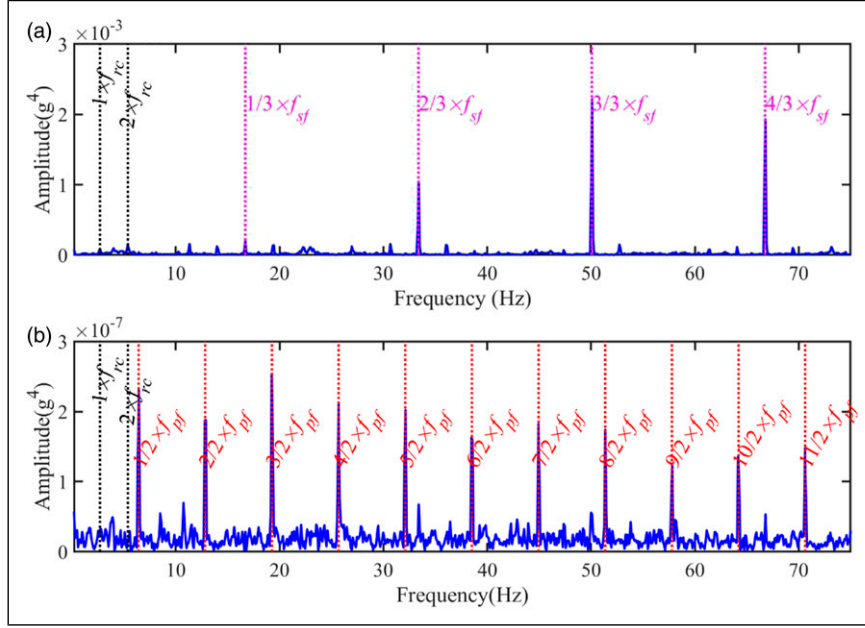


Figure 10. MSB-ESE of ORS vibrations for the faulty case at 60% speed and 90% load: (a) in the low-frequency band and (b) in the high-frequency band.

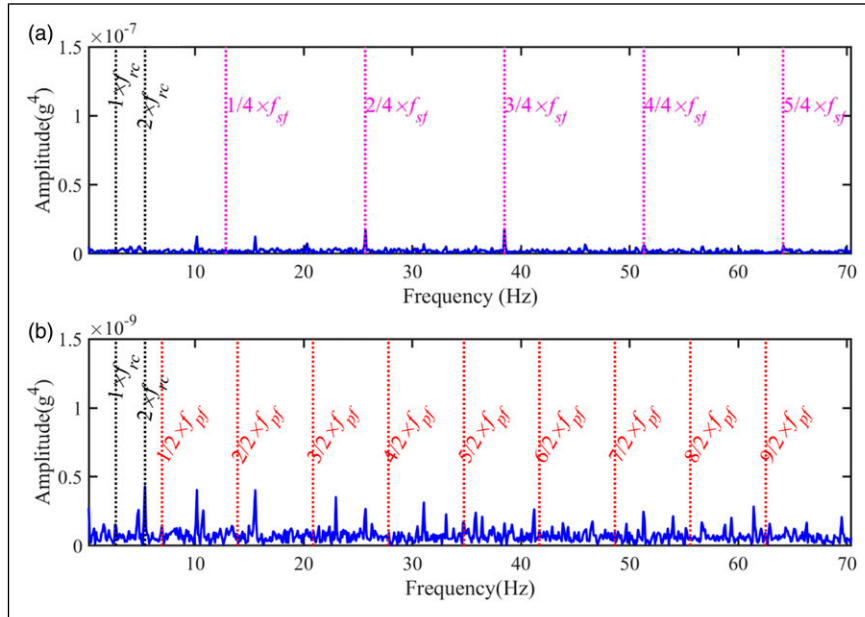


Figure 11. MSB-ESE of ORS vibrations for baseline case at 60% speed and 90% load: (a) in the low-frequency band and (b) in the high-frequency band.

MSB-ESE method and it also shows that ORS vibrations are much less influenced by transmission path.

Spectral Correlation Enhanced Envelope Spectrum

To further highlight the proposed method, the Spectral Correlation Enhanced Envelope Spectrum is also explored

because it can better enhance the non-zero cyclic components.³³ The Spectral Correlation Enhanced Envelope Spectrum is defined based on the Spectral Coherence which yields

$$\gamma(\alpha, f) = \frac{S(\alpha, f)}{\sqrt{S(0, f)S(0, f - \alpha)}} \quad (34)$$

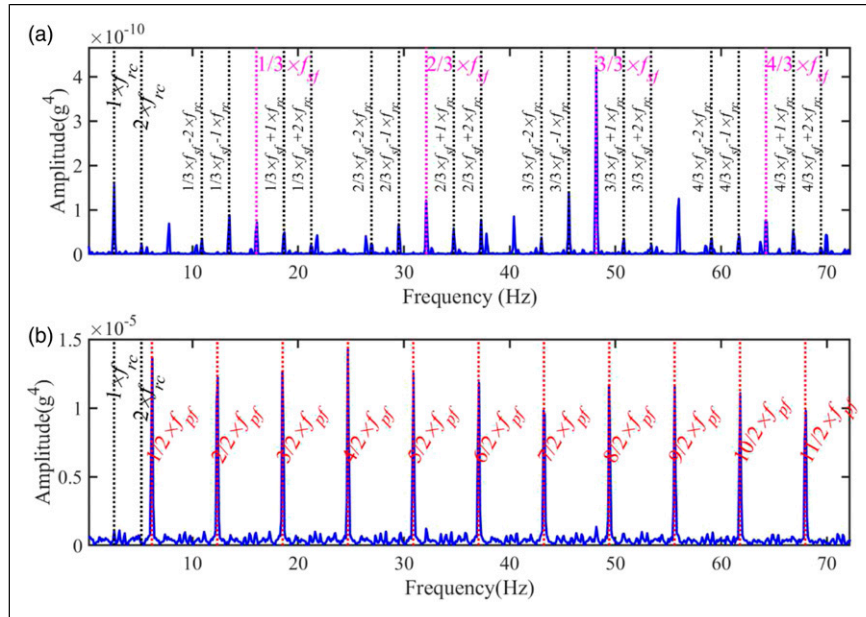


Figure 12. MSB-ESE of housing vibrations for faulty case: (a) in the low-frequency band and (b) in the high-frequency band.

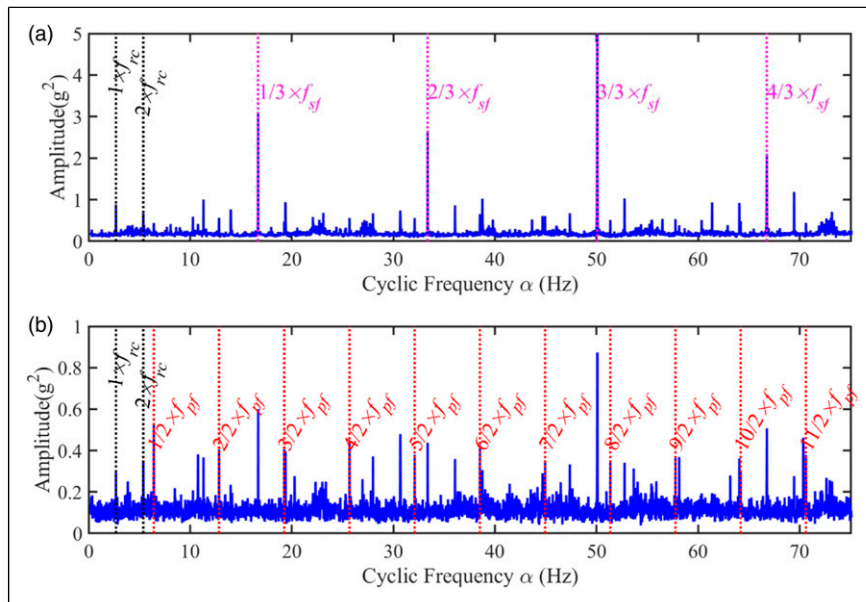


Figure 13. Spectral Correlation Enhanced Envelope Spectrum of ORS vibrations for the faulty case at 60% speed and 90% load: (a) in the low-frequency band and (b) in the high-frequency band.

$S(\alpha, f)$ is the Spectral Correlation that is defined in equation (18). The Spectral Coherence is a normalised version of the Spectral Correlation. The Spectral Correlation Enhanced Envelope Spectrum is obtained via the integral of the Spectral Coherence in a given frequency band $[f_1, f_2]$, yielding

$$S^{EES}(\alpha) = \int_{f_1}^{f_2} |\gamma(\alpha, f)| df \quad (35)$$

Figure 13 shows the Spectral Correlation Enhanced Envelope Spectrum for the faulty case and it can be seen that the results are similar to the conventional squared envelope

spectrum as presented in Figure 6. The sun gear fault can be identified clearly. However, the planet gear fault can be observed but mixed with other irrelevant components because of its noise inclusion and other interference. The fault frequencies and harmonics cannot be isolated from multiple discrete components and produce less reliable diagnostics.

Conclusions

To avoid the deficiency of conventional on-housing vibration measurements and analysis, this paper proposed a Modulation Signal Bispectrum Enhanced Squared Envelope method to extract the multiple fault harmonics in squared envelope analysis of vibration signals from a special ORS sensor on the carrier shaft of an epicyclic gearbox. The time-varying paths can be avoided by the ORS measurements and the MSB-ESE method can enhance the numerous fault harmonics induced by localised faults and suppress inevitable background noise in the squared envelope. The experimental studies demonstrate that the novel MSB-ESE can achieve a reliable diagnosis of compound planet and sun gear faults. In addition, this systematic sensing and analysis method can be used widely in condition monitoring of other rotating machines.

Acknowledgements

The authors would like to express their appreciation to the Centre for Efficiency and Performance Engineering (CEPE) at the University of Huddersfield for supporting the accomplishment of this research.

Declaration of Conflicting Interests

The author(s) declared no potential conflicts of interest with respect to the research, authorship, and/or publication of this article.

Funding

The author(s) received no financial support for the research, authorship, and/or publication of this article.

ORCID iD

Yuandong Xu  <https://orcid.org/0000-0003-4259-4727>

References

1. Qian P, Ma X, Zhang D, et al. Data-driven condition monitoring approaches to improving power output of wind turbines. *IEEE Trans Ind Electron* 2019; 66(8): 6012–6020. DOI: [10.1109/TIE.2018.2873519](https://doi.org/10.1109/TIE.2018.2873519).
2. Inalpolat M and Kahraman A. A theoretical and experimental investigation of modulation sidebands of planetary gear sets. *J Sound Vib* 2009; 323(3): 677–696. DOI: [10.1016/j.jsv.2009.01.004](https://doi.org/10.1016/j.jsv.2009.01.004).
3. Inalpolat M and Kahraman A. A dynamic model to predict modulation sidebands of a planetary gear set having manufacturing errors. *J Sound Vib* 2010; 329(4): 371–393. DOI: [10.1016/j.jsv.2009.09.022](https://doi.org/10.1016/j.jsv.2009.09.022).
4. Feng Z and Zuo MJ. Vibration signal models for fault diagnosis of planetary gearboxes. *J Sound Vib* 2012; 331(22): 4919–4939. DOI: [10.1016/j.jsv.2012.05.039](https://doi.org/10.1016/j.jsv.2012.05.039).
5. Blunt DM and Keller JA. Detection of a fatigue crack in a UH-60A planet gear carrier using vibration analysis. *Mech Syst Signal Process* 2006; 20(8): 2095–2111. DOI: [10.1016/j.ymsp.2006.05.010](https://doi.org/10.1016/j.ymsp.2006.05.010).
6. Feng Z, Liang M, Zhang Y, et al. Fault diagnosis for wind turbine planetary gearboxes via demodulation analysis based on ensemble empirical mode decomposition and energy separation. *Renew Energ* 2012; 47: 112–126. DOI: [10.1016/j.renene.2012.04.019](https://doi.org/10.1016/j.renene.2012.04.019).
7. Feng Z, Zuo MJ, Qu J, et al. Joint amplitude and frequency demodulation analysis based on local mean decomposition for fault diagnosis of planetary gearboxes. *Mech Syst Signal Process* 2013; 40(1): 56–75. DOI: [10.1016/j.ymsp.2013.05.016](https://doi.org/10.1016/j.ymsp.2013.05.016).
8. Wang T, Chu F and Han Q. Fault diagnosis for wind turbine planetary ring gear via a meshing resonance based filtering algorithm. *ISA Trans* 2017; 67: 173–182. DOI: [10.1016/j.isatra.2016.11.008](https://doi.org/10.1016/j.isatra.2016.11.008).
9. Feng Z, Chen X and Liang M. Joint envelope and frequency order spectrum analysis based on iterative generalized demodulation for planetary gearbox fault diagnosis under nonstationary conditions. *Mech Syst Signal Process* 2016; 76–77: 242–264. DOI: [10.1016/j.ymsp.2016.02.047](https://doi.org/10.1016/j.ymsp.2016.02.047).
10. Sawalhi N, Randall RB and Forrester D. Separation and enhancement of gear and bearing signals for the diagnosis of wind turbine transmission systems. *Wind Energy* 2014; 17(5): 729–743. DOI: [10.1002/we.1671](https://doi.org/10.1002/we.1671).
11. Hou B, Wang Y, Tang B, et al. A tacholess order tracking method for wind turbine planetary gearbox fault detection. *Measurement* 2019; 138: 266–277. DOI: [10.1016/j.measurement.2019.02.010](https://doi.org/10.1016/j.measurement.2019.02.010).
12. Guo Y, Zhao L, Wu X, et al. Tooth root crack detection of planet and sun gears based on resonance demodulation and vibration separation. *IEEE Trans Inst Meas* 2020; 69(1): 65–75. DOI: [10.1109/TIM.2019.2893011](https://doi.org/10.1109/TIM.2019.2893011).
13. Wang L, Shao Y and Cao Z. Optimal demodulation subband selection for sun gear crack fault diagnosis in planetary gearbox. *Measurement* 2018; 125: 554–563. DOI: [10.1016/j.measurement.2018.05.023](https://doi.org/10.1016/j.measurement.2018.05.023).
14. Mauricio A, Qi J and Gryllias K. Vibration-based condition monitoring of wind turbine gearboxes based on cyclostationary analysis. *J Eng Gas Turbines Powermar* 2019; 141(3): 031026. DOI: [10.1115/1.4041114](https://doi.org/10.1115/1.4041114).
15. Dziejciech K, Jablonski A and Dworakowski Z. Epicyclic gearbox fault detection by instantaneous circular pitch cycle map. *Mech Syst Signal Process* 2019; 121: 600–614. DOI: [10.1016/j.ymsp.2018.11.053](https://doi.org/10.1016/j.ymsp.2018.11.053).
16. Xu Y, Zhen D, Gu JX, et al. Autocorrelated envelopes for early fault detection of rolling bearings. *Mech Syst Signal*

- Process* 2021; 146: 106990. DOI: [10.1016/j.ymsp.2020.106990](https://doi.org/10.1016/j.ymsp.2020.106990).
17. Elasha F, Greaves M and Mba D. Planetary bearing defect detection in a commercial helicopter main gearbox with vibration and acoustic emission. *Struct Health Monit* 2018; 17(5): 1192–1212. DOI: [10.1177/1475921717738713](https://doi.org/10.1177/1475921717738713).
 18. Zhou L, Duan F, Corsar M, et al. A study on helicopter main gearbox planetary bearing fault diagnosis. *Appl Acoust* 2019; 147: 4–14. DOI: [10.1016/j.apacoust.2017.12.004](https://doi.org/10.1016/j.apacoust.2017.12.004).
 19. Lei Y, Lin J, Zuo MJ, et al. Condition monitoring and fault diagnosis of planetary gearboxes: A review. *Measurement* 2014; 48: 292–305. DOI: [10.1016/j.measurement.2013.11.012](https://doi.org/10.1016/j.measurement.2013.11.012).
 20. Fan Z and Li H. A hybrid approach for fault diagnosis of planetary bearings using an internal vibration sensor. *Measurement* 2015; 64: 71–80. DOI: [10.1016/j.measurement.2014.12.030](https://doi.org/10.1016/j.measurement.2014.12.030).
 21. Xu Y, Tang X, Feng G, et al. Orthogonal on-rotor sensing vibrations for condition monitoring of rotating machines. *J Dyn Monit Diagn* 2021; 1(1): 29–36. DOI: [10.37965/jdmd.v2i2.47](https://doi.org/10.37965/jdmd.v2i2.47).
 22. Rice SO. Mathematical analysis of random noise. *Bell Syst Tech J* 1944; 23(3): 282–332. DOI: [10.1002/j.1538-7305.1944.tb00874.x](https://doi.org/10.1002/j.1538-7305.1944.tb00874.x).
 23. Randall RB, Antoni J and Chobsaard S. The relationship between spectral correlation and envelope analysis in the diagnostics of bearing faults and other cyclostationary machine signals. *Mech Syst Signal Process* 2001; 15(5): 945–962. DOI: [10.1006/mssp.2001.1415](https://doi.org/10.1006/mssp.2001.1415).
 24. Randall RB, Antoni J and Chobsaard S. A comparison of cyclostationary and envelope analysis in the diagnostics of rolling element bearings. *IEEE Int Conf Acoust Speech Signal Process Proc* 2000; 6: 3882–3885. DOI: [10.1109/ICASSP.2000.860251](https://doi.org/10.1109/ICASSP.2000.860251).
 25. Fang Z-S and Xie N. An analysis of various methods for computing the envelope of a random signal. *Appl Ocean Res* 1995; 17(1): 9–19. DOI: [10.1016/0141-1187\(94\)00024-H](https://doi.org/10.1016/0141-1187(94)00024-H).
 26. Tayfun AM and Lo J-M. Wave envelope and related spectra. *J Waterway Port Coastal Ocean Eng* 1989; 115(4): 1989. DOI: [10.1061/\(ASCE\)0733-950X](https://doi.org/10.1061/(ASCE)0733-950X).
 27. Tian X, Xi Gu J, Rehab I, et al. A robust detector for rolling element bearing condition monitoring based on the modulation signal bispectrum and its performance evaluation against the Kurtogram. *Mech Syst Signal Process* 2018; 100: 167–187. DOI: [10.1016/j.ymsp.2017.07.037](https://doi.org/10.1016/j.ymsp.2017.07.037).
 28. Gu F, Wang T, Alwodai A, et al. A new method of accurate broken rotor bar diagnosis based on modulation signal bispectrum analysis of motor current signals. *Mech Syst Signal Process* 2015; 50–51: 400–413. DOI: [10.1016/j.ymsp.2014.05.017](https://doi.org/10.1016/j.ymsp.2014.05.017).
 29. Zhang R, Gu F, Mansaf H, et al. Gear wear monitoring by modulation signal bispectrum based on motor current signal analysis. *Mech Syst Signal Process* 2017; 94: 202–213. DOI: [10.1016/j.ymsp.2017.02.037](https://doi.org/10.1016/j.ymsp.2017.02.037).
 30. Gu F, Shao Y, Hu N, et al. Electrical motor current signal analysis using a modified bispectrum for fault diagnosis of downstream mechanical equipment. *Mech Syst Signal Process* 2011; 25(1): 360–372. DOI: [10.1016/j.ymsp.2010.07.004](https://doi.org/10.1016/j.ymsp.2010.07.004).
 31. Xu Y, Fu C, Hu N, et al. A phase linearisation-based modulation signal bispectrum for analysing cyclostationary bearing signals. *Struct Health Monit* 2020; 20: 1231–1246. DOI: [10.1177/1475921720949827](https://doi.org/10.1177/1475921720949827).
 32. Huang B, Feng G, Tang X, et al. A performance evaluation of two bispectrum analysis methods applied to electrical current signals for monitoring induction motor-driven systems. *Energies* 2019; 12(8): 1438. DOI: [10.3390/en12081438](https://doi.org/10.3390/en12081438).
 33. Antoni J, Xin G and Hamzaoui N. Fast computation of the spectral correlation. *Mech Syst Signal Process* 2017; 92: 248–277. DOI: [10.1016/j.ymsp.2017.01.011](https://doi.org/10.1016/j.ymsp.2017.01.011).

Appendix I

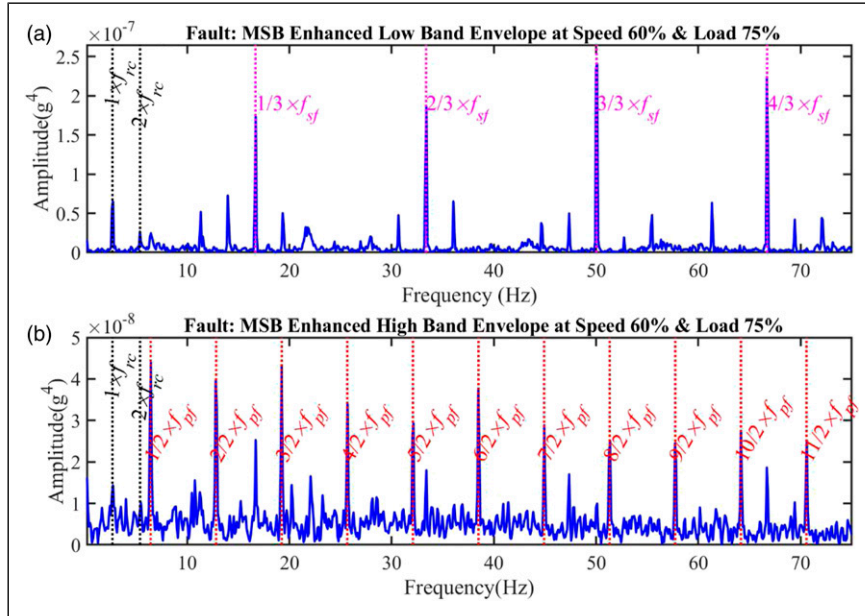


Figure A1. MSB-ESE of ORS vibrations at speed 60% and load 75% for the faulty case: (a) in the low-frequency band and (b) in the high-frequency band.

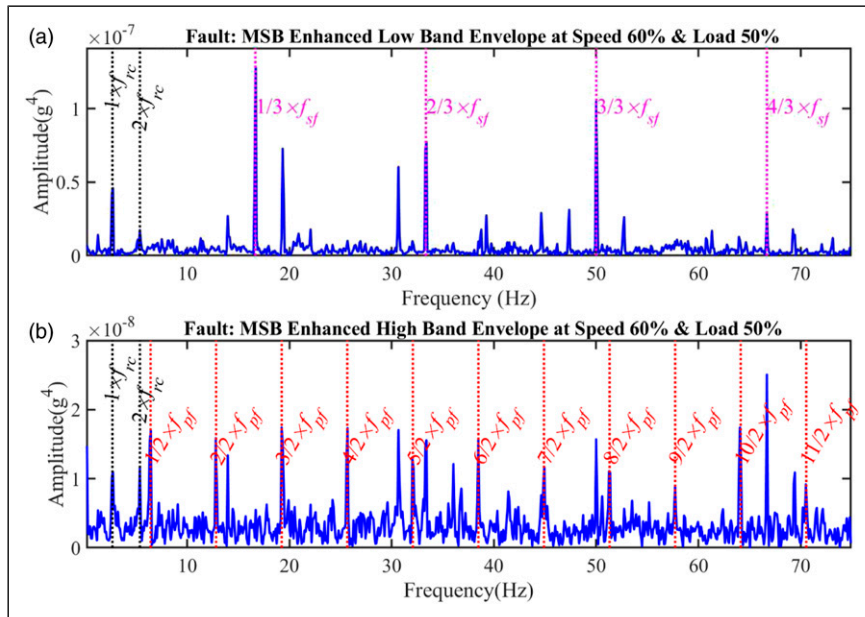


Figure A2. MSB-ESE of ORS vibrations at speed 60% and load 50% for the faulty case: (a) in the low-frequency band and (b) in the high-frequency band.

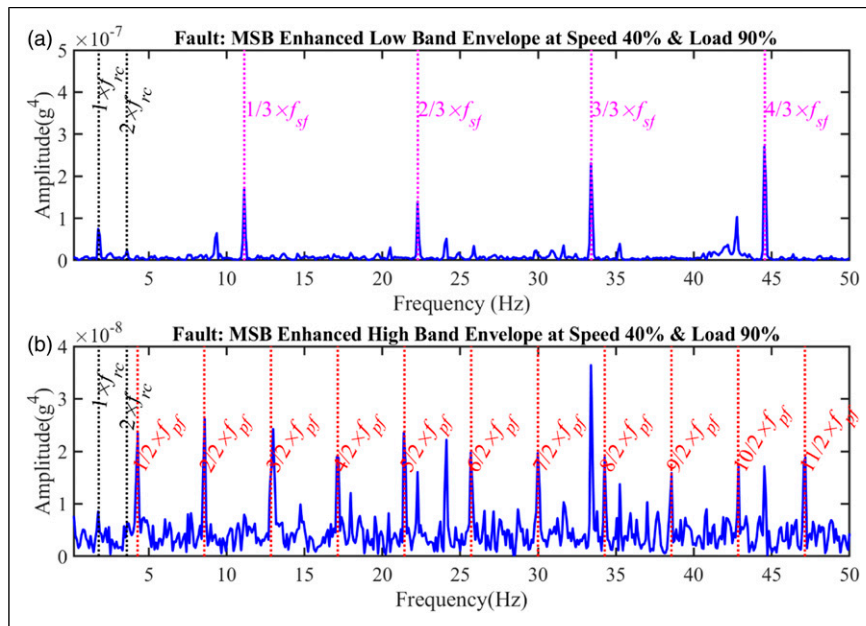


Figure A3. MSB-ESE of ORS vibrations at speed 40% and load 90% for the faulty case: (a) in the low-frequency band and (b) in the high-frequency band.

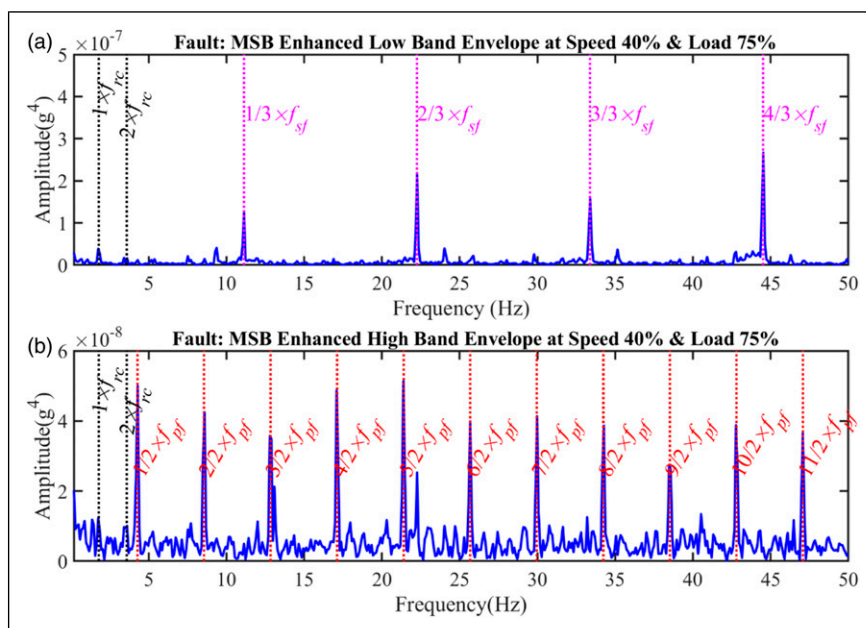


Figure A4. MSB-ESE of ORS vibrations at speed 40% and load 75% for the faulty case: (a) in the low-frequency band and (b) in the high-frequency band.

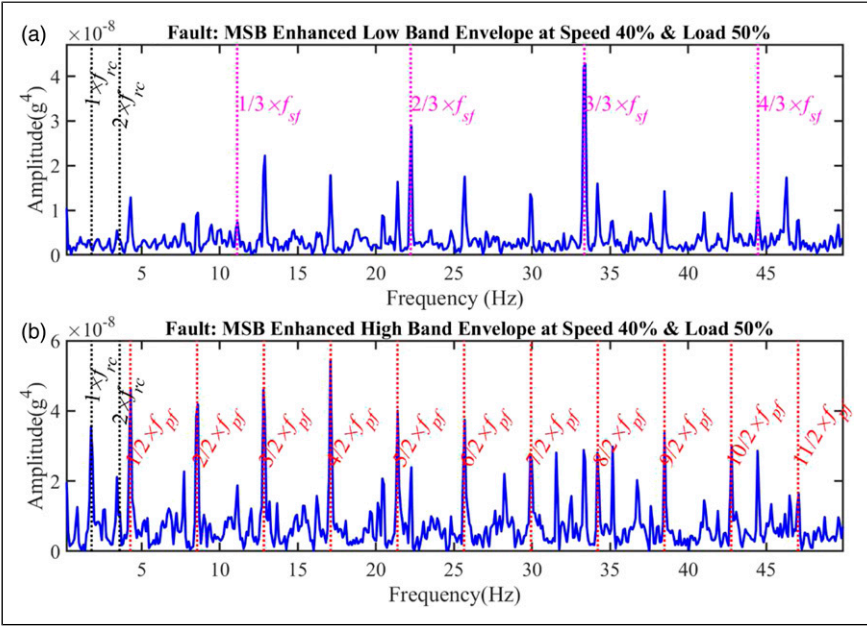


Figure A5. MSB-ESE of ORS vibrations at speed 40% and load 50% for the faulty case: (a) in the low-frequency band and (b) in the high-frequency band.